Spatial transcriptomics reveals focal induction of molecular responses and cellular interactions in the small intestine during *Heligmosomoides polygyrus* Infection.

Marta Campillo Poveda[1]*, Ross F Laidlaw[1], Olympia Hardy[1], Thomas D Otto[1], Rick M Maizels[1]

1 Wellcome Centre for Integrative Parasitology, School of Infection & Immunity, University of Glasgow, UK

* Corresponding Author: Marta Campillo Poveda. marta.campillopoveda@glasgow.ac.uk

Abstract:

The infective L3 larvae of *Heligmosomoides polygyrus* migrate to the small intestine where they take up residence in the submucosa, triggering the formation of complex granulomas around the parasite. Here, we employ spatial transcriptomics to elucidate the transcriptional intricacies and cell-cell interactions of the murine small intestine under both steady-state conditions and in response to *H. polygyrus* infection. Our findings unveil distinct transcriptional signatures in the crypt zone, villi, and granulomas, providing nuanced insights into the molecular dynamics of the host response to parasitic infection. Molecular characterization of *H. polygyrus* granulomas reveals unique cellular compositions within distinct clusters, shedding light on localized immune activation and cellular dynamics. Utilizing deconvolution techniques, we uncovered common and infection-specific signatures of cell type colocalization, and identified potential ligand-receptor pairs that may mediate communication between the granuloma tissue and the epithelial crypt cells. Additionally, our study highlights the upregulation of genes such as *Ccl9, Fcer1g* and *Tmsb4x* within granulomas, suggesting roles in type 2 inflammation, and genes (e.g *Reg3b* and *Mxra7*) associated with wound healing and tissue repair. These results not only enhance our understanding of the murine small intestine's transcriptional landscape but also provide a platform for exploring host-pathogen interactions. The comprehensive analysis presented here contributes to a holistic comprehension of tissue-specific responses during parasitic infections, offering valuable insights for targeted therapeutic interventions.

Introduction

Helminths, or parasitic worms, are amongst the most prevalent infectious agents afflicting individuals in developing nations, contributing to a global disease burden as severe as more recognized conditions like malaria and tuberculosis. Most helminth infections establish long-lived chronic parasitism, exacerbating the global health problem, and causing extensive morbidity in both humans and livestock (1, 2). A widely used model for intestinal helminth infections is *Heligmosomoides polygyrus*, a natural parasite of mice that can persist for many weeks or months in laboratory strains, defying the host's immune response (3, 4).

Intestinal helminth infections present intricate challenges when parasites, such as *H. polygyrus*, invade the submucosal tissues; here the concerted efforts of macrophages and granulocytes play a pivotal role in defence against invading parasites (5-8). Upon oral ingestion, larvae swiftly traverse the small intestine's epithelial barrier, establishing in the submucosal tissue before maturing into adults and returning to the intestinal lumen. Infection initiates a host type 2 immune response, which plays a crucial role in various physiological processes, ranging from safeguarding against parasites to contributing to metabolic adaptation, homeostasis, and tissue regeneration (9-12). The extensive localised and systemic properties of these responses highlight the recruitment of both immune and nonimmune cells into the type 2 effector orbit (13, 14), with the larvae rapidly encased in a granuloma surrounded and infiltrated by macrophages, neutrophils, and eosinophils (among other cell types) (7, 15). These carry out a variety of effector functions, like the production of IL-4 and IL-13 by eosinophils, which activate M2 macrophages in the muscularis, promoting disease tolerance (16) and mast cell degranulation, impacting epithelial permeability and smooth muscle activity (17).

Despite the host's robust immune response, *H. polygyrus* establishes long-term chronic infections attributed to its immunomodulatory effects. Most notable is its secretion of proteins that mimic the function of TGF-β (18), a pivotal regulator of the immune system through the induction of T regulatory cells, which inhibit the inflammatory effects of a variety of immune cells (19). Until recently, investigations into helminth immunomodulation predominantly focused on its downstream impacts on immune cell populations (18, 20-23). However, in more recent studies, attention has shifted towards unravelling the complex interactions between intestinal helminths and the epithelium (24-28). Particularly noteworthy are findings from the early stages of *H. polygyrus* infection, in which individual larvae mature in submucosal tissues within localised cysts or granulomas, typically 500-900 µm in size. During this phase, stem cells in the surrounding areas have been observed to undergo a "reversal" to a foetal-like repair phenotype (25). Additionally, these stem cells exhibit a compromised capacity to differentiate into various effector secretory cell subsets, including tuft, goblet, and Paneth cells (25, 27, 28), a finding that can be recapitulated in organoid cultures of intestinal stem cells exposed to *H. polygyrus* or its secreted products (27).

While the interactions and effects of the nematode on the immune system and epithelium are clearly extensive, it is important to better understand the spatial context in which host-parasite interactions occur and what changes occur across the infected tissue that may favour parasite establishment or clearance. In recent years, a powerful new set of techniques that combine transcriptomics with histology has emerged under the "Spatial Transcriptomics"

umbrella. These techniques assess gene transcription in individual cells or tissues using spatial resolution of <100 µm, accompanied by high-dimensional data collection. They enable the visualisation and quantitative analysis of the transcriptome in tissue sections, offering insights into cell-to-cell interactions, tissue heterogeneity, and functional organisation (29-31), making it an impressively powerful tool for better understanding the impact of host-parasite interaction.

In this study, spatial transcriptomics was employed to investigate the localised transcriptional profile within the intestinal epithelium and lamina propria of both naïve mice and mice infected with *H. polygyrus* over the first 7 days of infection (3). This report focuses on unravelling the immune responses triggered by *H. polygyrus* using spatial transcriptomics, pinpointing immune cell types within the granuloma, and delineating early gene expression in the submucosa associated with granuloma formation. Notably, our investigation unveiled a suite of transcriptional and morphological changes extending beyond conventional immune responses, providing new insights into the complex interplay between *H. polygyrus* and the intestinal environment and how the tissue environment responds to parasite invasion.

Materials and Methods

Mice and parasites

Eight-week-old female C57BL/6 mice purchased from Envigo UK and housed in individually ventilated cages were used throughout this study. All animal studies were performed under the UK Home Office Licence and approved by the University of Glasgow Ethical Review Board. Mice were infected by oral gavage with 400 infective third-stage larvae (L3) *H. polygyrus*, maintained as previously described (32). Mice were culled on day 7 post infection, the small intestine of each mouse was collected and gut rolls paraffin-embedded.

Tissue processing and library preparation

Processing small intestine tissue involved the removal of the gut-associated adipose tissue following which luminal contents were removed by washing with cold PBS. Starting from the most distal end, the small intestine was mounted onto a wooden skewer with the luminal side facing outwards. After 4h fixing in 4% NBF, tissue was cut longitudinally and rolled creating a gut roll with the distal small intestine at the centre. The roll was then left to fix overnight, followed by processing and embedding in paraffin (33). Five µm sections, that included at least one granuloma, were made using a microtome and placed on Visium 10x Genomics slides, fitting the 6.5mm² capture areas (Fig. 1A).

For analysis, slides with small intestine tissue from 7 days post-infection were stained with H&E, and imaged by NanoZoomer-SQ Digital slide scanner. Sequence libraries were processed per the manufacturer's instructions (10x Genomics, Visium Spatial Transcriptomic). After cDNA strand synthesis, cDNA was quantified using quantitative RT-PCR ABI 7500 Fast Real-Time PCR System and analysed with ABI 7500 Software 2.3 (Fig. 1A).

Sequencing and data processing

Visium libraries were sequenced using a P3 flow cell to an average of >200 million reads per sample on the NextSeq2000 instrument, paired-end 2x100bp. The sample images were then analysed and spots were assigned a metadata value according to the type of tissue the spot captured: Villi, Crypt, *H. polygyrus* (referred to as 'Worm') or Granuloma. Samples were mapped against the *Mus musculus* mm10 reference using 10X Genomics' Spaceranger version 2.1.1 on default parameters except for the loupe alignment JSON file, which was edited so that unlabelled spots were also included in the final mapping output.

Comparison of crypts and villi of *H. polygyrus* infected and naïve mice intestine

The mapped filtered_feature_bc_matrix h5 files were loaded into SCANPY (34) for processing and analysis. All unlabelled spots and genes which had expression in fewer than three spots were removed from the object prior to any pre-processing. Expression values of the samples were normalized and scaled. The top 2000 most variable genes, found using default parameters from SCANPY and the total mRNA counts in each spot, were regressed out. Principal component (PCs) analysis was carried out on the normalized, scaled expression data using only the genes identified as being highly variable. Later, the 7 days post *H. polygyrus* infection and naïve mouse Visium samples were integrated together using Harmony and a nearest neighbours graph was constructed using as many Harmony-adjusted PCs. This was deemed necessary based on the variance ratio plot of the PCs, with this graph being used as the basis for Leiden clustering and UMAP (35, 36). Marker genes of the resulting Leiden clusters were identified using SCANPY's rank_genes_groups function, using t-test to assess for statistical significance and Benjamini-Hochberg to adjust the p-value to correct for multiple-testing.

Characterising granulomas within *H. polygyrus* infected mice intestine

The mapped 7 days post *H. polygyrus* infection sample filtered_feature_bc_matrix h5 files were loaded into SCANPY for processing and analysis. All 4992 spots were designated as either unlabelled, Crypts or Villi and genes which had expression in less than three spots were removed from the object before any pre-processing. The nine distinct granuloma regions were identified using spectral clustering, carried out on the Visium coordinate space. Expression values of the samples were normalized, scaled and variable genes were found using default parameters from SCANPY. Finally, the total mRNA counts in each spot were regressed. PCs analysis was carried out on the normalized, scaled expression data using only the genes identified as being highly variable. A nearest neighbours (nn) graph was constructed using as many PCs as was deemed necessary based on the variance ratio plot of the PCs, with this graph being used as the basis for Leiden clustering and UMAP. Marker genes of the resulting Leiden clusters were identified using SCANPY's rank_genes_groups function, using t-test to assess for statistical significance and Benjamini-Hochberg to adjust the p-value to correct for multiple-testing.

Loupe browser

Loupe Browser (v.5.0.0; 10X Genomics) is a desktop application compatible with Windows and Macintosh operating systems. It facilitates the easy visualization and analysis of Visium

gene expression data. This software is employed for the identification of significant genes and cell types, as well as for exploring substructures within cell clusters. The Loupe Browser viewer utilizes single points representing cell barcodes. To visualize data within the Loupe Browser 2D space, Cell Ranger transfers Principal Components Analysis (PCA)-reduced data into a t-SNE (t-Stochastic Neighbour Embedding) plot. T-SNE is a nonlinear dimensionality reduction method with modifications by 10X Genomics. Loupe Browser includes a "Categories" mode, allowing users to label subpopulations of cells in the clustering plot with specific categories.

Unrolling the intestine gut roll

In the LoupeBrowser, two additional metadata csv files were generated: one with every spot manually annotated as ‘upper’ except for one spot, which was annotated as ‘centre’ and another where the bottommost spot layer of crypts was annotated as ‘basement’ and every other labelled spot annotated as ‘upper’. In the cases where spots annotated as ‘upper’ were not adjacent to any other ‘upper’ spots, as many unlabelled spots as required were labelled as ‘upper’ to connect them to the rest of the ‘upper’ spots contained on their layer (Supp Fig. 1 and 2).

The Visium datasets were loaded in as anndata objects into Python and split into two objects: spots designated as ‘upper’, and spots designated as ‘lower’ and for each object. Sklearn (37) was used to generate a radius nn graph with a radius of 33. To separate the different sections of the intestine in each object a random spot was chosen in the dataset to perform a depth-based search of the radius nn graph. This was repeated until all spots in the graph were visited. These spots were then given a ‘section’ designation of ‘section 0’ (where the number increases with every new search), and a new spot (unvisited by the depth -based search thus far) was chosen to repeat this process. This entire step of searching and clustering spots was repeated until all spots in the object had been visited by the search (Supp Fig. 1).

To identify which ‘upper’ and ‘basement’ sections need to be matched, same process was iterated through all the ‘basement’ sections. This trained a k-nearest neighbours (kNN) classifier by using sklearn on all the spots annotated as ‘upper’, plus the ‘section’ metadata as labels, and then predicting labels for each of the ‘basement’ section spots. Next, the resulting labels for the ‘basement’ section spots and the top two ‘upper’ section labels were tallied up. At this point, most were chosen as the possible matches for the current ‘basement’ section being considered. For each of the ‘upper’ sections being considered as a match for the current ‘basement’ section, the Euclidean distance (in the Visium coordinate space) from each spot to the centre spot defined in the metadata was calculated. These distances were then averaged, and the ‘upper’ section, which had the largest average distance, was matched with the current ‘basement’ section. These steps were repeated for all the ‘basement’ sections, resulting in a data frame where the first-row first-column value contains the label of the ‘upper’ section which is matched with the ‘basement’ section label contained in the first-row second-column. For a matched ‘basement’ and ‘upper’ section, if any of them contain less than ten spots, they are both removed from the analysis pipeline.

To recreate the length axis of the intestine, same processed were performed through the matched ‘basement’ and ‘upper’ sections and for each of the matched anndata objects. A nn graph from the Visium spatial coordinates using SCANPY’s ‘neighbours’ function was generated, using Euclidean distance as the distance metric, and using this nn graph as the

basis for performing Leiden clustering (35). Next, sklearn was used to create a distance and connectivity's radius nn graph (with radius set to 33) and to replace the neighbourhood information in the anndata object with this new information. The new neighbourhood information was then used as the basis for generating a PAGA graph (38) which was then subsequently used to make a Kamada & Kawai (KK) force-directed graph (39). The embeddings of the KK graph and the Leiden clustering calculated priorly were then used to perform trajectory inference with pySlingshot (40, 41). The resulting pseudotime values were used as the recreation of the original length axis. For both matched 'upper' and 'basement' sections, there were two possible start points for the trajectories therefore, to ensure that both sections have similar starting points, the starting clusters were chosen based on minimising the distance between the 'upper' and 'basement' starting clusters. As the lengths can sometimes be asynchronous between the 'upper' and 'basement' sections, performing kNN regression with sklearn was used to training the regressor on the length values of the 'upper' section. This was followed by performing regression with this trained model on the 'basement' section. The length for each of the matched sections was scaled between 0 and the maximum Euclidean distance between spots on the 'upper' or 'basement' sections, multiplied by the max distance divided by 100 then doubled. The two matched 'basement' and 'upper' section anndata objects were finally merged (Supp Fig. 1).

To recreate the depth axis, the depth value of all the 'basement' spots in a matched anndata object was assigned to be 0. For every 'upper' spot, the closet 'basement' spot was identified in the new length axis. This set the depth of the respective 'upper' spot to be the Euclidean distance between it and its closest 'basement' spot as determined previously. The depth values of a matched anndata object are then scaled between 0 and the maximum of the length axis of that anndata object divided by 15 (Supp Fig. 1).

Preparing the single-cell RNA sequencing reference datasets

The raw expression matrices and metadata of the Xu et al 92019) and Haber et al (2016) scRNA-seq data were downloaded and loaded into Seurat (42). For the Xu data, more quality control of the samples was carried out. This consisted of removing cells with remarkably high/low nFeature_counts and also those with a high percentage of mitochondrial reads per cell. The cut-off values can be seen by viewing the relevant code on our github. The metadata of the Xu cells was then simplified, with the cell types being designated as 'low UMI' being merged with their regular UMI counterparts and specific subsets of cell type e.g. 'DC (Cd103+ Cd11b+)', 'DC (Cd103+ Cd11b-)' and 'DC (Cd103- C2)' being simplified as just 'DC'. Nonimmune cells were also removed from the Xu datasets. The Xu and Haber Seurat objects were then merged and converted into h5ad format.

Cell2location analysis of *H. polygyrus* infected and naïve mice intestine

For setting up the model of the Xu and Haber merged scRNA-seq dataset, we used the sequencing run of each of the datasets as the 'batch_key' and included the condition of the datasets (e.g. allergy, parasite infected, naive/control) as a categorical covariate. The training parameters for the training of the Visium slide model in cell2location (43) were chosen as follows. Within both the day 7 and naïve Visium samples there was variation in total UMI counts that could not be explained by the tissue, thus the RNA detection sensitivity parameter was set to 20, as per the recommendation of the cell2location authors. The number of cells

per location was chosen to be 50, based on visual observation of the scanned slides. The models were trained on a GPU with 80gb of RAM. The 5% quantile cell abundance was stored in the Visium anndata objects and used for all subsequent analysis and visualisation.

Non-negative factorization (NMF) analysis in cell2location was carried out, using the concatenation of the new length and depth coordinates and the original Visium coordinates as the spatial basis for the NMF. For the day 7 sample, 7 factors were created while five factors were created for the naïve sample.

Cellular communication inference of *H. polygyrus* infection in the murine intestine

Spatial niches defined by the NMF factorisation analysis yielded three distinct spatially resolved neighbourhoods termed the villi, upper crypt, lower crypt and granuloma niche. Spots assigned these labels were fed into CellChat (v.2.1.1) alongside the spatial coordinates from the full resolution tissue image to allow resulting interactions to be within spatial constraints. The conversion of spatial coordinates from pixels to micrometres was calculated using the ratio of the theoretical spot size set to 55um over the number of pixels that cover the diameter of the spot. In addition to this, the communication probability of two cells interacting was also restricted with a contact range set to 100 as recommended by the CellChat 10X Visium workflow. The CellChat database used was set to the organism '*mouse*' and all functional interaction annotations were used except those classified as '*Non-protein Signalling*' to avoid the inclusion of interactions involving synaptic signalling which lies outside the context of the murine intestinal tissue.

Package versions

Python version 3.10.12 was used with the following packages: Pandas – 1.5.3, Numpy – 1.23.0, SCANPY – 1.9.3, anndata – 0.8.0, squidpy – 1.3.1, scipy – 1.10.1, sklearn – 1.3.0, cell2location – 0.1.3

R version 4.2.2 was used with the following packages: Seurat – 4.3.0, harmony – 1.2.0, SeuratDisk – 0.0.0.9020, CellChat – 2.1.1

When training the cell2location models on GPUs, Python version 3.10.9 was along with the following package versions: cell2location – 0.1.4, scipy – 1.10.0, SCANPY – 1.9.6, scikit-learn – 1.2.1, numpy – 1.23.4, pandas – 2.1.4

Results

I. Spatial transcriptomics revealed distinct transcriptional signatures in the different regions of the murine small intestine at a steady state.

To profile the transcriptomic landscape of the small intestine tissue in naïve mice, we employed the Visium (10X Genomics) platform to conduct spatial transcriptomics on formalin-fixed gut rolls (Fig. 1). The analysis was specifically focused on three factors or categories, that encapsulates the fundamental structure of the small intestine under naïve and *H. polygyrus* infections, the crypt zone (including the lamina propria and the crypts), the villi and the granuloma (only present in *H. polygyrus* infected mice). Each of the 4992 spots was assigned a different category by hand, using the Loupe Browser (10X Genomics). The naïve Visium dataset was filtered by removing spots that were left unlabelled and removing genes that had expression in 3 or fewer spots. This left us with expression values from 3560 valid spots across 19465 genes which had, on average, 32087 unique molecular identifiers (UMI) per spot.

The transcriptomic signatures of known cell-specific markers unveiled the same spatial distribution to the different areas of the gut as those assigned by hand (Supp. Fig. 3. Genes such as the intestinal stem cell marker *Smoc2* and growth regulator *Rack1* (44, 45) (Supp. Fig. 3A, B) define the crypt zone, where the stem cells differentiate, and the early epithelial cells start to express markers of differentiation. On the other hand, the villus signature is characterized by villin genes *Vil1*, *Ezr,* myosin and fimbrin genes *Myo15b* and *Pls1* (46, 47), and class 2 major histocompatibility complex (MHC II) genes *H2-Q1* and *H2-Q2*, which help maintain the tight junctions of the enterocytes and facilitate the presentation of antigens respectively (48, 49) (Supp. Fig. 3A, C).

II. Spatial transcriptomics revealed distinct transcriptional signatures in the small intestine during H. polygyrus infection.

When the infective L3 larvae of *H. polygyrus* are ingested and migrate to the small intestine, they cross the epithelial barrier to take up residence in the submucosa. There a complex granuloma forms around the parasites, where they mature into L4 larvae and then into adulthood. To assess the changes to the mucosa that occur following parasite exposure, we compared uninfected mice to those taken 7 days post *H. polygyrus* infection. In the infected sample, as before, each of the spots was assigned a different category by hand, using the Loupe Browser (10X Genomics) and filtering of the sample was carried out in a similar fashion to the naive, with the resulting dataset having 3964 valid spots across 19465 genes, with a mean mRNA count of 10077 per spot.

When combining the overall transcriptional landscapes of the naïve and *H. polygyrus* infected small intestines, we observed a clear division of the spots annotated as the different categories, separating the crypt zones and the villi in both samples (Fig. 2A). Furthermore, when we then compare the two datasets, there is a conspicuous division between naïve and infected samples (Fig. 2B). This finding illustrates the profound transformation of gene expression in the small intestine following *H. polygyrus* infection in mice.

We then focussed separately on the crypt and villous areas of the small intestine in naïve and infected murine guts and identified specific genetic signatures in each of the cell populations during infection. Specifically, in infected crypts compared to naïve crypts, there is a decrease in genes associated with secreted components involved in maintaining intestinal homeostasis like *Zg16*, *Muc13, Itln1* and *Fcgbp*, which help protect the intestine against bacteria colonisation (50-52). In the infected crypts there is also a reduction in factors that maintain the integrity of the intestinal barrier such as *Epcam* and *Pls1* (53) (Fig. 2C). Overall, the infected crypts showed downregulation across the board of key stem cell genes (Supp. Fig. 4B). On the other hand, the genes which are upregulated in the infected crypts (Fig. 2D) collectively suggest a switch in other cellular processes. In the infected mice, elevated expression is seen of pyroptosis associated factor *Gsdmc4,* which has shown to be upregulated in IL-4 treated and *Nippostrongylus brasiliensis* infected mouse intestinal cells (54), and of phospholipase A2 family member *Pla2g4c,* which is involved in and required for killing of larval *H. polygyrus* (55). Finally, we also see higher expression in a variety of oncogenes (*Src* and *Ptpn18*) (56, 57) as well as cell adhesion proteins (*Cldn3*, *Cdh17*) (58, 59) which may signify the proliferation of epithelial cells and their responses to the presence of the parasite which may involve modification in tight junctions at this early stage of infection.

III. Molecular Characterization of the H. polygyrus granuloma and the surrounding small intestine.

Next, we focused on the day 7 post-infection tissue, more particularly on the granulomas, the area surrounding the worm (Fig. 3A). We compared the transcriptomic signatures of all the granulomas in comparison to the rest of the intestinal tissue (Fig. 3B). As previously noted, *Arg1* (arginase-1) is highly expressed in the granulomas (15) and is closely associated with alternatively activated (M2) macrophages, as is also the case for *Retnla* (encoding RELM-α). While *Fcer1g,* the IgE receptor, has previously been linked to macrophages in tumour settings, its prominence in the granuloma suggests a broader role in tissue responses. Perhaps most remarkable is the high expression of *Tmsb4x*, encoding thymosin beta-4, a small protein that may regulate inflammation in septicaemia (60). Additional upregulated genes are involved in extracellular matrix (ECM) remodelling and more general regulation of antigen presentation and inflammatory processes. ECM remodelling is indicated by the upregulation of *Fn1*, *Col1a1*, and *Ctsb*. Antigen presentation and immune response modulation are suggested by genes like *C1qa*, *Tnfaip2*, and *Psap*. The presence of *Apoe* and *Cyba* points to potential roles in lipid metabolism and oxidative stress regulation (61, 62). These upregulated genes collectively imply a coordinated response involving immune cells, tissue repair, and modulation of inflammatory processes within the granuloma microenvironment.

Finally, we focused only on the granulomas, which were clustered based on their transcriptomic profile, 3 different clusters were identified (Fig. 3C-D) at the chosen resolution. Cluster 0 spots represent granulomas in which no larva is visible, either because the adult is already in the lumen or because the section is offset with respect to the worm. The upregulation of the identified genes suggests the involvement of a diverse array of cell types. *H2-Q2* indicates the presence of immune cells capable of MHC class II antigen presentation, as well as involved in interferon responses (*Ifi27l2b*), and immune regulation (*Clec2h*). Furthermore, the upregulation of *Vil1*, *Zg16*, and *Krt20* suggests the presence of epithelial cells that may contribute to the structure within the granuloma (63). Interestingly, one of the

marker genes of cluster 0 granulomas is *Zg16*, which is conversely down-regulated in infected villi (Fig. 2F, Fig. 3D).

The observed gene expression specific to Cluster 1 suggests a multifaceted immune response in the core of the granulomas, in the areas close to the parasite. This transcriptional signature encompasses features of both type 1 and type 2 immunity. The upregulation of pro-inflammatory genes such as M cell products *Tnfaip2* and *Ccl9* (64) and IgE receptor *Fcer1g* (65), while the involvement of genes such as *Arg1*, *Basp1*, *Fn1*, *Emilin1*, and *Psap* (66-68) points towards tissue repair, extracellular matrix remodelling, and regulatory mechanisms characteristic of type 2 immunity. Additionally, the upregulation of *C1qa* implies complement system activation, which can contribute to both inflammatory and immune-regulatory processes (69). The dynamic interplay of these immune components suggests a balanced and coordinated host response to *H. polygyrus*, reflecting the complexity of *in vivo* immune reactions with overlapping features of type 1 and type 2 immunity (Fig. 3D).

Furthermore, Cluster 2, is only represented by one single granuloma (Fig. 3D and Suppl. Fig. 5). In this cluster, we find a variety of genes (e.g. *Reg3b, Reg3g, Agr2*) indicating resolution and repair of the cellular environment (30, 70, 71), together with *Mxra7*, encoding Matrix remodelling associated 7 protein implicated in wound-healing (72). Additionally, RNA processing and translation-related genes (*Pcbp2, Eef1b2, Eef1a1, Sf3b1, Rbm5*) suggest heightened cellular activity (73-75). Histone genes (*Hist1h4h, Hist1h1c, Hist1h3c*) point to chromatin remodelling, impacting gene expression in various cell types (76). Moreover, genes associated with protein quality control and apoptosis (*Agr2, Pdcd4*) imply roles in maintaining cellular homeostasis, involving multiple cell types responding to stress (Fig. 3E) (77, 78).

IV. Cell-to-cell interactions predicted and signalling pathways.

Unlike solid tissues, to lay out the intestine effectively on the Visium capture area a gut roll needs to be created. This has the consequence of a distorted spatial axis, where the distance and adjacency of the spots on the Visium capture area are not comparable to those of the tissue's biological context (Supp. Fig. 2A, B). Furthermore, as the dimensions of a roll exceed the 6.5 x 6.5mm capture area, some sections of the intestine are not included, creating discontinuous sections of the intestine (Supp. Fig. 2C). Thus, before analysing the data, we first clustered the intestine into distinct continuous sections (Supp. Fig. 2D) and recreated the original biological distance and adjacency (Fig. 4B, Supp. Fig. 1).

Having recreated the original biological spatial context of the intestine, we next identified the cell types present and their distribution across the spatial axis. In bulk RNA-seq data cell type abundance can be estimated by cell type deconvolution, where a scRNA-seq reference dataset is used to estimate the proportions of different cell types within a bulk sample (79). To deconvolute the Visium spot data, we used cell2location (43), a method for deconvoluting spatial transcriptomic data which builds expression profiles of cell types from a reference scRNA-seq dataset and uses these profiles to decompose the transcripts within spots into the supplied cell types from the scRNA-seq dataset.

We integrated two scRNA-seq datasets of immune and non-immune cells from the intestines of mice respectively from Xu et al., 2019 and Haber et al., 2017 (80, 81) to ensure there would be sufficient representation of the immune and epithelial cell types that comprise the

intestine. Leveraging histological annotations, we focused on one of the proximal parts of the intestine, the duodenum, of the gut roll (Fig. 4A, Supp. Fig. 6). Ensuring that we preserved spatial localisation of the tissue we used our calculated spatial embeddings containing our unrolled length and depth axis (Fig. 4B). and the original Visium spatial coordinates, to ensure adjacent segments in the Visium space are separated from each other. After applying non-negative matrix factorization (see methods) to identify which cell types colocalize together in the same regions of the tissue, we observed that across the 7 days post *H. polygyrus* infection and naïve mouse intestine, there are common signatures of cell type colocalization, especially among the non-immune cells.

Within the deepest spot layer of the crypts, one factor (1) is driven by transit amplifying (TA) cells, stem cells and T cells and another directly above this bottom-most layer which is almost entirely driven by enterocyte progenitors (Fig. 4A, C, D & Supp. Fig. 7A-C). Extending toward the mucosa, factor 4 colocalises enterocytes, B cells, innate lymphoid cells (ILC) 1 and 2, NK cells and gamma-delta T cells (Fig. 4A, C, D & Supp. Fig. 7A-C). Focusing on colocalization signatures that are specific to either the naive or infected mice, the analysis revealed a factor (9) largely composed of macrophage, neutrophil, plasmacytoid DC, mast cell and lymphoid tissue inducer cells that were localised in the intestinal granulomas (Fig. 4A, C, D). This contrasts with the naïve condition in which macrophages and neutrophils are distributed across the intestine (Supp. Fig. 8, 9).

Following cell type characterisation of the spatially resolved murine gut we examined the differential expression of genes across the spatial niches that reflect an intense cellular immune response during infection (Fig. 5A). Gene set enrichment analysis of differentially expressed genes in the granuloma niche during *H. polygyrus* infection points to general activation by cytokines, including specifically type II interferon which has previously been implicated at this time point (25, 82) (Fig. 5A). To further dissect potential drivers of this inflammatory response we analysed spatially constrained cellular interactions based on complementary ligand-receptor pairings localised to the spatial niches defined surrounding the granuloma. The highest number of predicted interactions was seen between cells residing in the lower crypt niche and the site of the granuloma (Fig. 5B & Fig. 4C, D). Enriched predicted signalling pathways between these niches included tissue remodelling through interactions with the ECM and various proteoglycans such as *Sdc1/4* and *Cd36*. In addition, a striking enrichment of cytokine signalling pathways through *Ccl6/7/8* may be associated with the activated myeloid and lymphocyte populations enriched in the granuloma and acting on the crypt (Fig. 5D, G). These chemokines promote immune cell migration and activation to the site of inflammation and bind to receptors *Ccr2* and *Ccr5*. This suggests that in areas of the lower crypt surrounding the granuloma we have increased cytokine signalling that promotes migration of macrophages, basophils and lymphocytes to the site of infection.

Within the spatial niche of the granuloma, there is further evidence of monocyte migration, immune cell activation and cytokine production. Increased *Angptl4* expression is also seen, suggesting hypoxia at the site of the granuloma could be triggered by the influx of various immune cells in the inflamed tissue. Furthermore, we observe expression of *Trem2* to various apolipoproteins suggesting a small subset of intestinal macrophages involved in suppressing the immune response and a role in clearance through phagocytosis directly at the site of infection (Fig. 5E, H). This is supported by functional analysis of upregulated ligand-receptor interactions within the granuloma niche that are involved in phagocytotic processes in the

context of the inflammatory response (Fig. 5H). Similarly, when we examine upregulated cellular interactions between the lower crypt and the granuloma, we see functional enrichment of extensive tissue remodelling and cell migration (Fig. 5I) supporting immune cell chemotaxis and disturbance to the cell matrix in *H. polygyrus* infection.

Discussion

Spatial transcriptomics has emerged as a powerful tool to unravel the intricacies of gene expression patterns within the complex architecture of tissues. In this study, we employed the Visium platform to conduct spatial transcriptomics on murine small intestine tissues, providing a comprehensive view of the transcriptional landscape during steady-state conditions and in response to *H. polygyrus* infection. Furthermore, we uncover the localisation of various cell types within the context of steady state and helminth-infected intestines and extract the cell-cell interactions that take place between them.

Upon *H. polygyrus* infection, dynamic transcriptional changes were observed in the small intestine, particularly within the granuloma and surrounding areas. One such change is the apparent upregulation of tight junction genes in the helminth infected gut compared to the naive, which could impair the host's ability to increase fluid egress as part of the 'weep and sweep' response against helminths. In addition, as *H. polygyrus* infection can lead to the suppression of differentiated specialist epithelial cells like goblet, paneth and tuft cells (25, 27, 28), this may explain attenuated expression of specific stem cell differentiation genes of the crypt areas.

The transcriptomic analysis at day 7 post-infection revealed a multifaceted immune response, with distinct granuloma signatures categorized into clusters based on the distance to the parasite, which may be indicative of a longitudinal response to the parasite from active inflammation to resolution of the immune response. While the parasite is still present within the granuloma, a variety of type 2 immune response factors are expressed, including *Fcer1g* and products of M2 phenotype macrophages like *Arg1* and *Fn1*, all of which are associated with the clearance/expulsion of parasites. Once the parasite is no longer detected in the granuloma, there is a return towards homeostasis, with an increase in extracellular matrix remodelling and maintenance of the intestinal barrier through keratin deposition.

While many of the cell types found to be co-localized around and within granuloma niches (like macrophages, neutrophils, dendritic cells and CD4+ T cells) have been shown to be associated with helminth-induced granulomas, mast cells, pDCs and Lymphoid Tissue inducer (LTi) cells have not (6). Eosinophils are among the immune cell types associated with granulomas but as they are not present in the reference scRNA-seq dataset they were excluded from the analysis. Given that mast cells and eosinophils are both granulocytes there might be some mislabelling of eosinophils as mast cells. The presence of pDCs within the granuloma is unusual, given their classical role as a mediator of anti-viral immune responses. This result could be misidentification of the cluster as pDCs, however, the expression of pDC markers *Siglech*, *Klk1* and *Cox6a2* (83, 84), was indeed highest in the clusters annotated as 'pDC' (Supp. Fig. 10). There is some evidence to suggest that pDCs are beneficial in a response to intestinal parasite infection. While pDCs are not required for Th2 immune responses to *Schistosoma mansoni* (*S. mansoni*) in the liver and spleen (85), Webb and colleagues 2021 (86) showed that pDCs help the immune system mount an optimal type 2 immune response to *S. mansoni* eggs in the intestine, however, their participation was limited to the mesenteric lymph nodes and the granulomas were not investigated. The role of pDCs as a granuloma associated cell type during helminth infection thus needs to be investigated to assess whether this finding is novel or a quirk of the deconvolution process.

Despite potential limitations of deconvolution approaches it allowed us to leverage spatially resolved neighbourhoods with existing single cell data to predict cell-to-cell interactions of spatial niches within the small intestine. Common signatures of cell type colocalization were identified, particularly in the crypts and villi, emphasizing the coordinated organization of various cell types within specific tissue regions. Specific colocalization patterns in *H. polygyrus* infection, particularly in the granulomas, highlighted the dynamic cellular interactions occurring during the host response to parasitic infection. In contrast, in the steady-state there is negligible activity from immune cells and the interactome is rather associated with epithelial cell differentiation and maintaining tissue integrity of the intestine. Thus, this landscape is dramatically altered in response to parasitic infection and the formation of granulomas. The dominant type I interferon response is driven by the recruitment of antigen presenting cells to the site of infection and outline the dual functionality of macrophages in driving the immune response but also resolution during *H. polygyrus* infection.

Although our study demonstrates the heterogeneity of the host response across different spatial compartments of the intestine during *H. polygyrus* infection, the advent of higher-resolution spatial sequencing techniques would allow insight into the transcriptomic landscape of individual cells, and potentially the helminth itself, within their native spatial context. This will offer insights into cell types, their spatial distribution, potential heterogeneity within specific regions, and interactions with the parasite, enabling a comprehensive characterization of the dynamic host-pathogen interplay. Future work includes integrating additional time points of *H. polygyrus* infection in the murine intestine to map the spatial-temporal dynamics of the interplay of the host immune system and gut epithelia. These insights gained from our study lay the groundwork for future investigations into the molecular mechanisms driving host defence and tissue responses during parasitic infections. To conclude, this report highlights the main strengths of spatial transcriptomics, which is to access and unravel previously inaccessible details, paving the way for a more in-depth comprehension of the molecular and spatial dimensions of host immune responses and tissue-specific adaptations to parasitic challenges.

Code availability

The code to replicate this analysis can be found at the following github repository: https://github.com/No2Ross/Visium_Hpolgyrus_gut

Acknowledgements

We thank Dr Juan Quintana and Claire Ciancia for their excellent technical assistance and expertise. The authors gratefully acknowledge Glasgow Polyomics (University of Glasgow) for their support and assistance.

Funding

M.C.P. and R.M.M.are supported by the Wellcome Trust through an Investigator Award to RMM (Ref 219530), and the Wellcome Trust core-funded Wellcome Centre for Integrative Parasitology (Ref: 104111), including an Early Career Researchers Futurescope grant from the Centre. R.F.L was funded by the Medical Research Council through their Precision Medicine DTP (MRC grant number: MR/N013166/1). O.H was funded by the Research into Inflammatory Arthritis Centre Versus Arthritis UK, based in the Universities of Glasgow, Birmingham, Newcastle and Oxford.

Author contributions

All authors helped shape the research, analysis, and manuscript. The study was designed by M.C.P. and R.M.M. with input from T.O. M.C.P., O.H and R.F.L generated the data, performed the analysis and drafted the manuscript figures and text. R.M.M and T.O provided critical feedback and edited the manuscript prior to submission.

Declaration of interest

The authors declare no competing interests.

References

1. Hotez PJ, Brindley PJ, Bethony JM, King CH, Pearce EJ, Jacobson J. Helminth infections: the great neglected tropical diseases. J Clin Invest. 2008;118(4):1311-21.
2. Morgan ER, Aziz NA, Blanchard A, Charlier J, Charvet C, Claerebout E, et al. 100 Questions in Livestock Helminthology Research. Trends Parasitol. 2019;35(1):52-71.
3. Monroy FG, Enriquez FJ. Heligmosomoides polygyrus: a model for chronic gastrointestinal helminthiasis. Parasitol Today. 1992;8(2):49-54.
4. Reynolds LA, Filbey KJ, Maizels RM. Immunity to the model intestinal helminth parasite Heligmosomoides polygyrus. Semin Immunopathol. 2012;34(6):829-46.
5. Lechner A, Bohnacker S, Esser-von Bieren J. Macrophage regulation & function in helminth infection. Semin Immunol. 2021;53:101526.
6. Anthony RM, Rutitzky LI, Urban JF, Jr., Stadecker MJ, Gause WC. Protective immune mechanisms in helminth infection. Nat Rev Immunol. 2007;7(12):975-87.
7. Hewitson JP, Filbey KJ, Esser-von Bieren J, Camberis M, Schwartz C, Murray J, et al. Concerted activity of IgG1 antibodies and IL-4/IL-25-dependent effector cells trap helminth larvae in the tissues following vaccination with defined secreted antigens, providing sterile immunity to challenge infection. PLoS Pathog. 2015;11(3):e1004676.
8. Chen F, El-Naccache DW, Ponessa JJ, Lemenze A, Espinosa V, Wu W, et al. Helminth resistance is mediated by differential activation of recruited monocyte-derived alveolar macrophages and arginine depletion. Cell Rep. 2022;38(2):110215.
9. Gieseck RL, 3rd, Wilson MS, Wynn TA. Type 2 immunity in tissue repair and fibrosis. Nat Rev Immunol. 2018;18(1):62-76.
10. Pelly VS, Kannan Y, Coomes SM, Entwistle LJ, Rückerl D, Seddon B, et al. IL-4-producing ILC2s are required for the differentiation of T(H)2 cells following Heligmosomoides polygyrus infection. Mucosal Immunol. 2016;9(6):1407-17.
11. Filbey KJ, Grainger JR, Smith KA, Boon L, van Rooijen N, Harcus Y, et al. Innate and adaptive type 2 immune cell responses in genetically controlled resistance to intestinal helminth infection. Immunol Cell Biol. 2014;92(5):436-48.
12. Lloyd CM, Snelgrove RJ. Type 2 immunity: Expanding our view. Sci Immunol. 2018;3(25).
13. Inclan-Rico JM, Rossi HL, Herbert DR. "Every cell is an immune cell; contributions of non-hematopoietic cells to anti-helminth immunity". Mucosal Immunol. 2022;15(6):1199-211.
14. Ariyaratne A, Finney CAM. Eosinophils and Macrophages within the Th2-Induced Granuloma: Balancing Killing and Healing in a Tight Space. Infect Immun. 2019;87(10).
15. Anthony RM, Urban JF, Jr., Alem F, Hamed HA, Rozo CT, Boucher JL, et al. Memory T(H)2 cells induce alternatively activated macrophages to mediate protection against nematode parasites. Nat Med. 2006;12(8):955-60.
16. Ahrends T, Aydin B, Matheis F, Classon CH, Marchildon F, Furtado GC, et al. Enteric pathogens induce tissue tolerance and prevent neuronal loss from subsequent infections. Cell. 2021;184(23):5715-27.e12.
17. Shimokawa C, Kanaya T, Hachisuka M, Ishiwata K, Hisaeda H, Kurashima Y, et al. Mast Cells Are Crucial for Induction of Group 2 Innate Lymphoid Cells and Clearance of Helminth Infections. Immunity. 2017;46(5):863-74.e4.

18. Johnston CJC, Smyth DJ, Kodali RB, White MPJ, Harcus Y, Filbey KJ, et al. A structurally distinct TGF-β mimic from an intestinal helminth parasite potently induces regulatory T cells. Nat Commun. 2017;8(1):1741.
19. Sanjabi S, Oh SA, Li MO. Regulation of the Immune Response by TGF-β: From Conception to Autoimmunity and Infection. Cold Spring Harb Perspect Biol. 2017;9(6).
20. Maizels RM. Regulation of immunity and allergy by helminth parasites. Allergy. 2020;75(3):524-34.
21. Harris NL, Loke P. Recent Advances in Type-2-Cell-Mediated Immunity: Insights from Helminth Infection. Immunity. 2017;47(6):1024-36.
22. de Los Reyes Jiménez M, Lechner A, Alessandrini F, Bohnacker S, Schindela S, Trompette A, et al. An anti-inflammatory eicosanoid switch mediates the suppression of type-2 inflammation by helminth larval products. Sci Transl Med. 2020;12(540).
23. Maizels RM, Gause WC. Targeting helminths: The expanding world of type 2 immune effector mechanisms. J Exp Med. 2023;220(10).
24. Artis D, Grencis RK. The intestinal epithelium: sensors to effectors in nematode infection. Mucosal Immunol. 2008;1(4):252-64.
25. Nusse YM, Savage AK, Marangoni P, Rosendahl-Huber AKM, Landman TA, de Sauvage FJ, et al. Parasitic helminths induce fetal-like reversion in the intestinal stem cell niche. Nature. 2018;559(7712):109-13.
26. Coakley G, Harris NL. Interactions between macrophages and helminths. Parasite Immunol. 2020;42(7):e12717.
27. Drurey C, Lindholm HT, Coakley G, Poveda MC, Löser S, Doolan R, et al. Intestinal epithelial tuft cell induction is negated by a murine helminth and its secreted products. J Exp Med. 2022;219(1).
28. Karo-Atar D, Ouladan S, Javkar T, Joumier L, Matheson MK, Merritt S, et al. Helminth-induced reprogramming of the stem cell compartment inhibits type 2 immunity. J Exp Med. 2022;219(9).
29. Williams CG, Lee HJ, Asatsuma T, Vento-Tormo R, Haque A. An introduction to spatial transcriptomics for biomedical research. Genome Med. 2022;14(1):68.
30. Parigi SM, Larsson L, Das S, Ramirez Flores RO, Frede A, Tripathi KP, et al. The spatial transcriptomic landscape of the healing mouse intestine following damage. Nat Commun. 2022;13(1):828.
31. Wood CS, Pennel KAF, Leslie H, Legrini A, Cameron AJ, Melissourgou-Syka L, et al. Spatially Resolved Transcriptomics Deconvolutes Prognostic Histological Subgroups in Patients with Colorectal Cancer and Synchronous Liver Metastases. Cancer Res. 2023;83(8):1329-44.
32. Camberis M, Le Gros G, Urban J, Jr. Animal model of Nippostrongylus brasiliensis and Heligmosomoides polygyrus. Curr Protoc Immunol. 2003;Chapter 19:Unit 19.2.
33. Bialkowska AB, Ghaleb AM, Nandan MO, Yang VW. Improved Swiss-rolling Technique for Intestinal Tissue Preparation for Immunohistochemical and Immunofluorescent Analyses. J Vis Exp. 2016(113).
34. Wolf FA, Angerer P, Theis FJ. SCANPY: large-scale single-cell gene expression data analysis. Genome Biol. 2018;19(1):15.
35. Traag VA, Waltman L, van Eck NJ. From Louvain to Leiden: guaranteeing well-connected communities. Scientific Reports. 2019;9(1):5233.
36. McInnes L, Healy J, Melville J. UMAP: Uniform Manifold Approximation and Projection for Dimension Reduction. . Journal of Open Source Software. 2018; 3(861).

37. Pedregosa F, Varoquaux G, Gramfort A, Michel V, Thirion B, Grisel O, et al. Scikit-learn: Machine Learning in Python. Journal of Machine Learning Research. 2011;12(85):2825−30.
38. Wolf FA, Hamey FK, Plass M, Solana J, Dahlin JS, Göttgens B, et al. PAGA: graph abstraction reconciles clustering with trajectory inference through a topology preserving map of single cells. Genome Biology. 2019;20(1):59.
39. Kamada T, Kawai S. An algorithm for drawing general undirected graphs. Information Processing Letters. 1989;31(1):7-15.
40. Street K, Risso D, Fletcher RB, Das D, Ngai J, Yosef N, et al. Slingshot: cell lineage and pseudotime inference for single-cell transcriptomics. BMC Genomics. 2018;19(1):477.
41. Moss J. Python implementation of the slingshot pseudotime algorithm. GitHub: https://github.com/mossjacob/pyslingshot
42. Hao Y, Stuart T, Kowalski MH, Choudhary S, Hoffman P, Hartman A, et al. Dictionary learning for integrative, multimodal and scalable single-cell analysis. Nature Biotechnology. 2023.
43. Kleshchevnikov V, Shmatko A, Dann E, Aivazidis A, King HW, Li T, et al. Cell2location maps fine-grained cell types in spatial transcriptomics. Nat Biotechnol. 2022;40(5):661-71.
44. Jang BG, Kim HS, Bae JM, Kim WH, Kim HU, Kang GH. SMOC2, an intestinal stem cell marker, is an independent prognostic marker associated with better survival in colorectal cancers. Sci Rep. 2020;10(1):14591.
45. Cheng ZF, Pai RK, Cartwright CA. Rack1 function in intestinal epithelia: regulating crypt cell proliferation and regeneration and promoting differentiation and apoptosis. Am J Physiol Gastrointest Liver Physiol. 2018;314(1):G1-g13.
46. Drenckhahn D, Dermietzel R. Organization of the actin filament cytoskeleton in the intestinal brush border: a quantitative and qualitative immunoelectron microscope study. J Cell Biol. 1988;107(3):1037-48.
47. Friederich E, Pringault E, Arpin M, Louvard D. From the structure to the function of villin, an actin-binding protein of the brush border. Bioessays. 1990;12(9):403-8.
48. Beyaz S, Chung C, Mou H, Bauer-Rowe KE, Xifaras ME, Ergin I, et al. Dietary suppression of MHC class II expression in intestinal epithelial cells enhances intestinal tumorigenesis. Cell Stem Cell. 2021;28(11):1922-35.e5.
49. Wosen JE, Mukhopadhyay D, Macaubas C, Mellins ED. Epithelial MHC Class II Expression and Its Role in Antigen Presentation in the Gastrointestinal and Respiratory Tracts. Front Immunol. 2018;9:2144.
50. Bergström JH, Birchenough GM, Katona G, Schroeder BO, Schütte A, Ermund A, et al. Gram-positive bacteria are held at a distance in the colon mucus by the lectin-like protein ZG16. Proc Natl Acad Sci U S A. 2016;113(48):13833-8.
51. Nonnecke EB, Castillo PA, Akahoshi DT, Goley SM, Bevins CL, Lönnerdal B. Characterization of an intelectin-1 (Itln1) knockout mouse model. Front Immunol. 2022;13:894649.
52. Ehrencrona E, van der Post S, Gallego P, Recktenwald CV, Rodriguez-Pineiro AM, Garcia-Bonete MJ, et al. The IgGFc-binding protein FCGBP is secreted with all GDPH sequences cleaved but maintained by interfragment disulfide bonds. J Biol Chem. 2021;297(1):100871.
53. Chen G, Yang Y, Liu W, Huang L, Yang L, Lei Y, et al. EpCAM is essential for maintenance of the small intestinal epithelium architecture via regulation of the expression and

localization of proteins that compose adherens junctions. Int J Mol Med. 2021;47(2):621-32.
54. Xi R, Montague J, Lin X, Lu C, Lei W, Tanaka K, et al. Up-regulation of gasdermin C in mouse small intestine is associated with lytic cell death in enterocytes in worm-induced type 2 immunity. Proc Natl Acad Sci U S A. 2021;118(30).
55. Entwistle LJ, Pelly VS, Coomes SM, Kannan Y, Perez-Lloret J, Czieso S, et al. Epithelial-Cell-Derived Phospholipase A(2) Group 1B Is an Endogenous Anthelmintic. Cell Host Microbe. 2017;22(4):484-93.e5.
56. Bjorge JD, Jakymiw A, Fujita DJ. Selected glimpses into the activation and function of Src kinase. Oncogene. 2000;19(49):5620-35.
57. Li C, Li SZ, Huang XC, Chen J, Liu W, Zhang XD, et al. PTPN18 promotes colorectal cancer progression by regulating the c-MYC-CDK4 axis. Genes Dis. 2021;8(6):838-48.
58. Baumholtz AI, Gupta IR, Ryan AK. Claudins in morphogenesis: Forming an epithelial tube. Tissue Barriers. 2017;5(4):e1361899.
59. Panarelli NC, Yantiss RK, Yeh MM, Liu Y, Chen YT. Tissue-specific cadherin CDH17 is a useful marker of gastrointestinal adenocarcinomas with higher sensitivity than CDX2. Am J Clin Pathol. 2012;138(2):211-22.
60. Liao Y, Xiao N, Wang X, Dai S, Wang G. Promoting effect of Tmsb4x on the differentiation of peripheral blood mononuclear cells to dendritic cells during septicemia. Int Immunopharmacol. 2022;111:109002.
61. Mahley RW. Apolipoprotein E: cholesterol transport protein with expanding role in cell biology. Science. 1988;240(4852):622-30.
62. Lee MY, Griendling KK. Redox signaling, vascular function, and hypertension. Antioxid Redox Signal. 2008;10(6):1045-59.
63. Wang Y, Srinivasan K, Siddiqui MR, George SP, Tomar A, Khurana S. A novel role for villin in intestinal epithelial cell survival and homeostasis. J Biol Chem. 2008;283(14):9454-64.
64. Wood MB, Rios D, Williams IR. TNF-α augments RANKL-dependent intestinal M cell differentiation in enteroid cultures. Am J Physiol Cell Physiol. 2016;311(3):C498-507.
65. Turner H, Kinet JP. Signalling through the high-affinity IgE receptor Fc epsilonRI. Nature. 1999;402(6760 Suppl):B24-30.
66. Jablonski KA, Amici SA, Webb LM, Ruiz-Rosado Jde D, Popovich PG, Partida-Sanchez S, Guerau-de-Arellano M. Novel Markers to Delineate Murine M1 and M2 Macrophages. PLoS One. 2015;10(12):e0145342.
67. Capuano A, Pivetta E, Baldissera F, Bosisio G, Wassermann B, Bucciotti F, et al. Integrin binding site within the gC1q domain orchestrates EMILIN-1-induced lymphangiogenesis. Matrix Biology. 2019;81:34-49.
68. Kashiba M, Terashima M, Sagawa T, Yoshimura S, Yamamoto Y. Prosaposin knockdown in Caco-2 cells decreases cellular levels of coenzyme Q10 and ATP, and results in the loss of tight junction barriers. J Clin Biochem Nutr. 2017;60(2):81-5.
69. Pendse M, De Selle H, Vo N, Quinn G, Dende C, Li Y, et al. Macrophages regulate gastrointestinal motility through complement component 1q. Elife. 2023;12.
70. Bergström JH, Berg KA, Rodríguez-Piñeiro AM, Stecher B, Johansson ME, Hansson GC. AGR2, an endoplasmic reticulum protein, is secreted into the gastrointestinal mucus. PLoS One. 2014;9(8):e104186.
71. Qu M, Xiong L, Lyu Y, Zhang X, Shen J, Guan J, et al. Establishment of intestinal organoid cultures modeling injury-associated epithelial regeneration. Cell Res. 2021;31(3):259-71.

72. Shen Y, Ning J, Zhao L, Liu W, Wang T, Yu J, Wang Y. Matrix remodeling associated 7 proteins promote cutaneous wound healing through vimentin in coordinating fibroblast functions. Inflammation and Regeneration. 2023;43(1):5.
73. Dever TE, Dinman JD, Green R. Translation Elongation and Recoding in Eukaryotes. Cold Spring Harb Perspect Biol. 2018;10(8).
74. Ghanem LR, Kromer A, Silverman IM, Ji X, Gazzara M, Nguyen N, et al. Poly(C)-Binding Protein Pcbp2 Enables Differentiation of Definitive Erythropoiesis by Directing Functional Splicing of the Runx1 Transcript. Mol Cell Biol. 2018;38(16).
75. Soni K, Jagtap PKA, Martínez-Lumbreras S, Bonnal S, Geerlof A, Stehle R, et al. Structural basis for specific RNA recognition by the alternative splicing factor RBM5. Nature Communications. 2023;14(1):4233.
76. Martire S, Banaszynski LA. The roles of histone variants in fine-tuning chromatin organization and function. Nat Rev Mol Cell Biol. 2020;21(9):522-41.
77. Delom F, Mohtar MA, Hupp T, Fessart D. The anterior gradient-2 interactome. Am J Physiol Cell Physiol. 2020;318(1):C40-c7.
78. Pin G, Huanting L, Chengzhan Z, Xinjuan K, Yugong F, Wei L, et al. Down-Regulation of PDCD4 Promotes Proliferation, Angiogenesis and Tumorigenesis in Glioma Cells. Front Cell Dev Biol. 2020;8:593685.
79. Newman AM, Steen CB, Liu CL, Gentles AJ, Chaudhuri AA, Scherer F, et al. Determining cell type abundance and expression from bulk tissues with digital cytometry. Nat Biotechnol. 2019;37(7):773-82.
80. Haber AL, Biton M, Rogel N, Herbst RH, Shekhar K, Smillie C, et al. A single-cell survey of the small intestinal epithelium. Nature. 2017;551(7680):333-9.
81. Xu H, Ding J, Porter CBM, Wallrapp A, Tabaka M, Ma S, et al. Transcriptional Atlas of Intestinal Immune Cells Reveals that Neuropeptide α-CGRP Modulates Group 2 Innate Lymphoid Cell Responses. Immunity. 2019;51(4):696-708.e9.
82. Progatzky F, Shapiro M, Chng SH, Garcia-Cassani B, Classon CH, Sevgi S, et al. Regulation of intestinal immunity and tissue repair by enteric glia. Nature. 2021;599(7883):125-30.
83. Blasius AL, Colonna M. Sampling and signaling in plasmacytoid dendritic cells: the potential roles of Siglec-H. Trends in Immunology. 2006;27(6):255-60.
84. Valente M, Collinet n, Vu Manh TP, Popoff D, Rahmani K, Naciri K, et al. Novel mouse models based on intersectional genetics to identify and characterize plasmacytoid dendritic cells. Nature Immunology. 2023;24(4):714-28.
85. Lundie RJ, Webb LM, Marley AK, Phythian-Adams AT, Cook PC, Jackson-Jones LH, et al. A central role for hepatic conventional dendritic cells in supporting Th2 responses during helminth infection. Immunol Cell Biol. 2016;94(4):400-10.
86. Webb LM, Phythian-Adams AT, Costain AH, Brown SL, Lundie RJ, Forde-Thomas J, et al. Plasmacytoid Dendritic Cells Facilitate Th Cell Cytokine Responses throughout Schistosoma mansoni Infection. Immunohorizons. 2021;5(8):721-32.

Figures

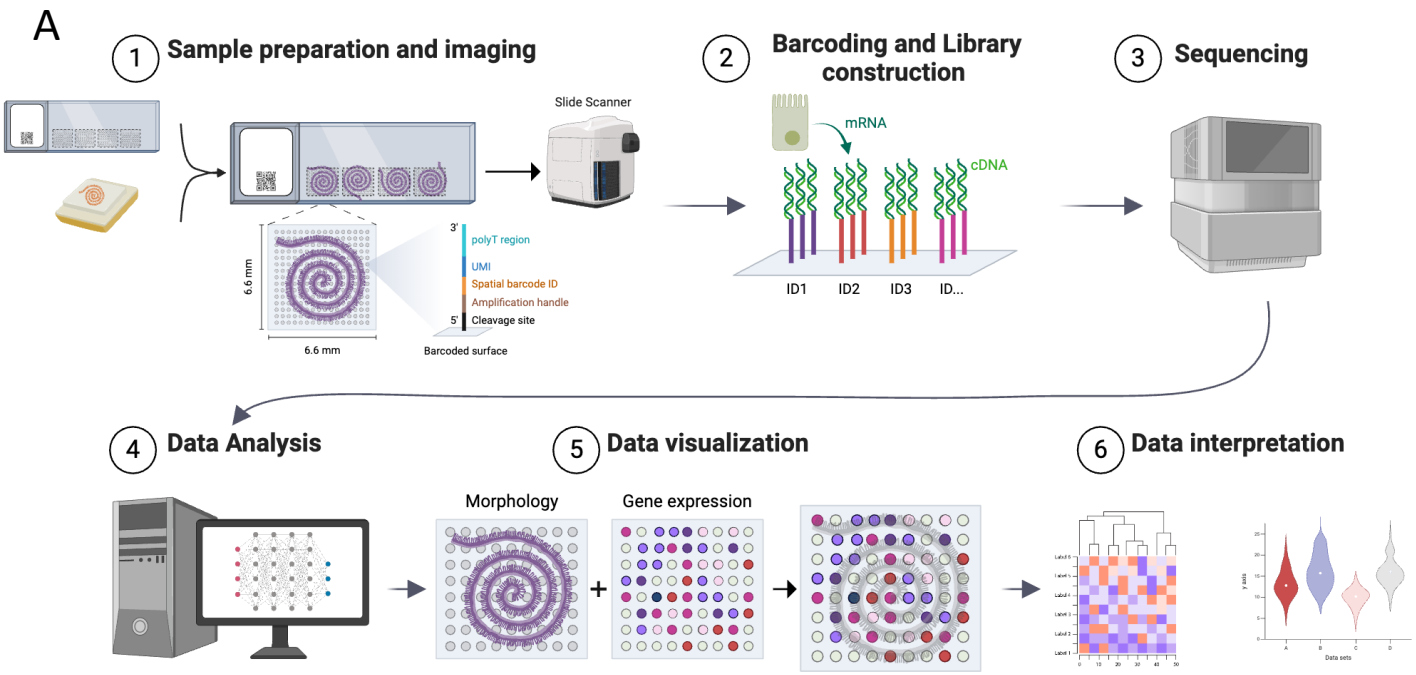

Figure 1: Tissue preparation and sequencing. A) Schematics of the experiment: mouse small intestine was processed for gut rolls in Formalin-Fixed Paraffin-Embedded (FFPE) blocks and further spatial transcriptomic with Visium 10X technology.

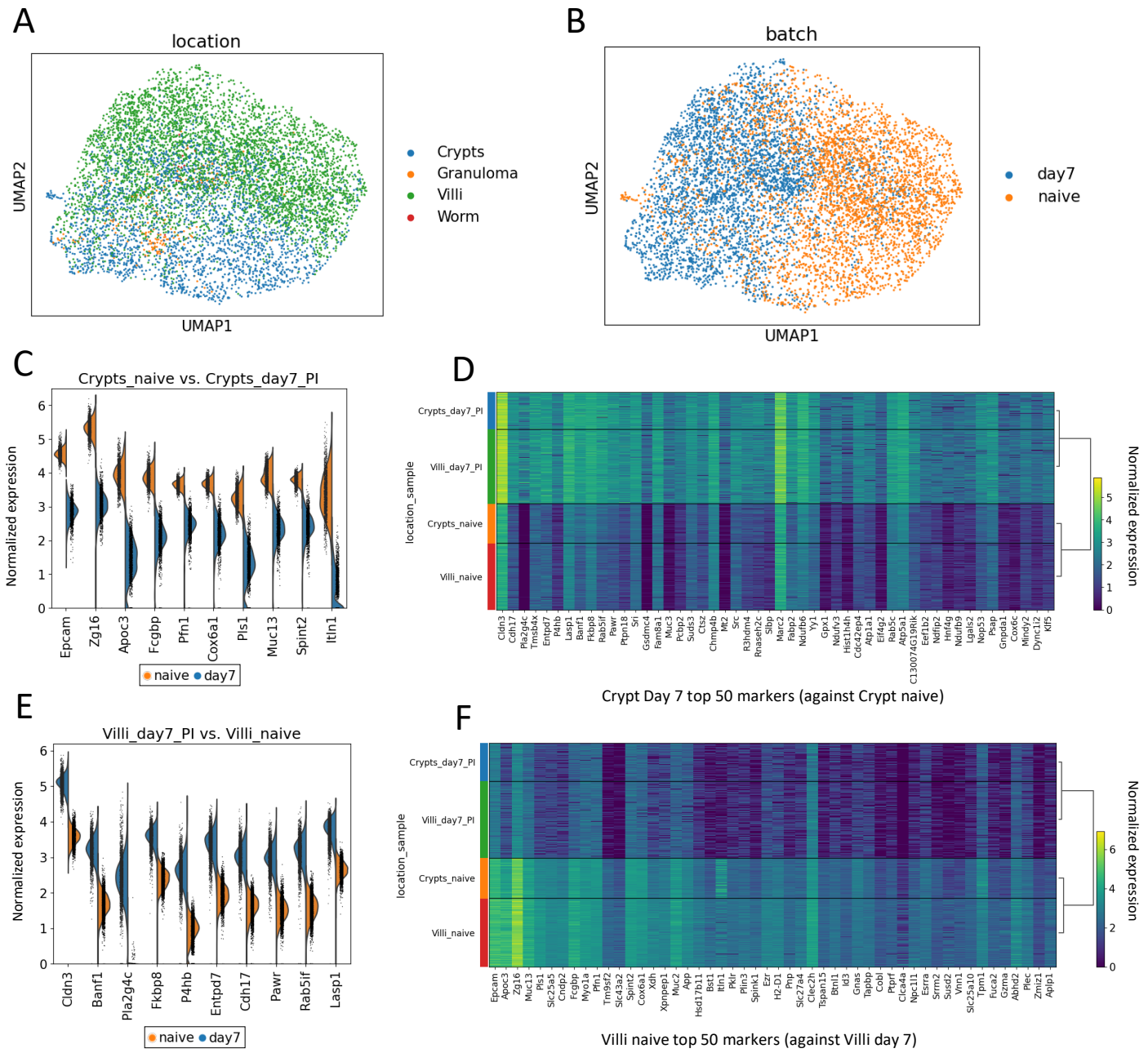

Figure 2. Transcriptomic differences between naïve and *H. polygyrus* infected mouse intestine. A) UMAP based on Harmony integration of naïve and 7 days post *H. polygyrus* infection Visium datasets, coloured by the tissue location of the spots. B) UMAP based on Harmony integration of naïve and 7 days post *H. polygyrus* infection Visium datasets coloured by the sample origin of each of the dots (Naïve or 7 days post *H. polygyrus infection*). C-E) Violin plots of the expression of the top 10 differentially expressed genes in naïve and day 7 crypt and villi. Orange violin plots show normalized expression of naïve spots and blue violin plots show normalized expression of day 7 post infection spots. D-F) Heatmaps showing the normalized expression of the top 50 differentially expressed genes in the crypt and villi tissue areas on day 7 post infection vs naïve, ranked by SCANPY score.

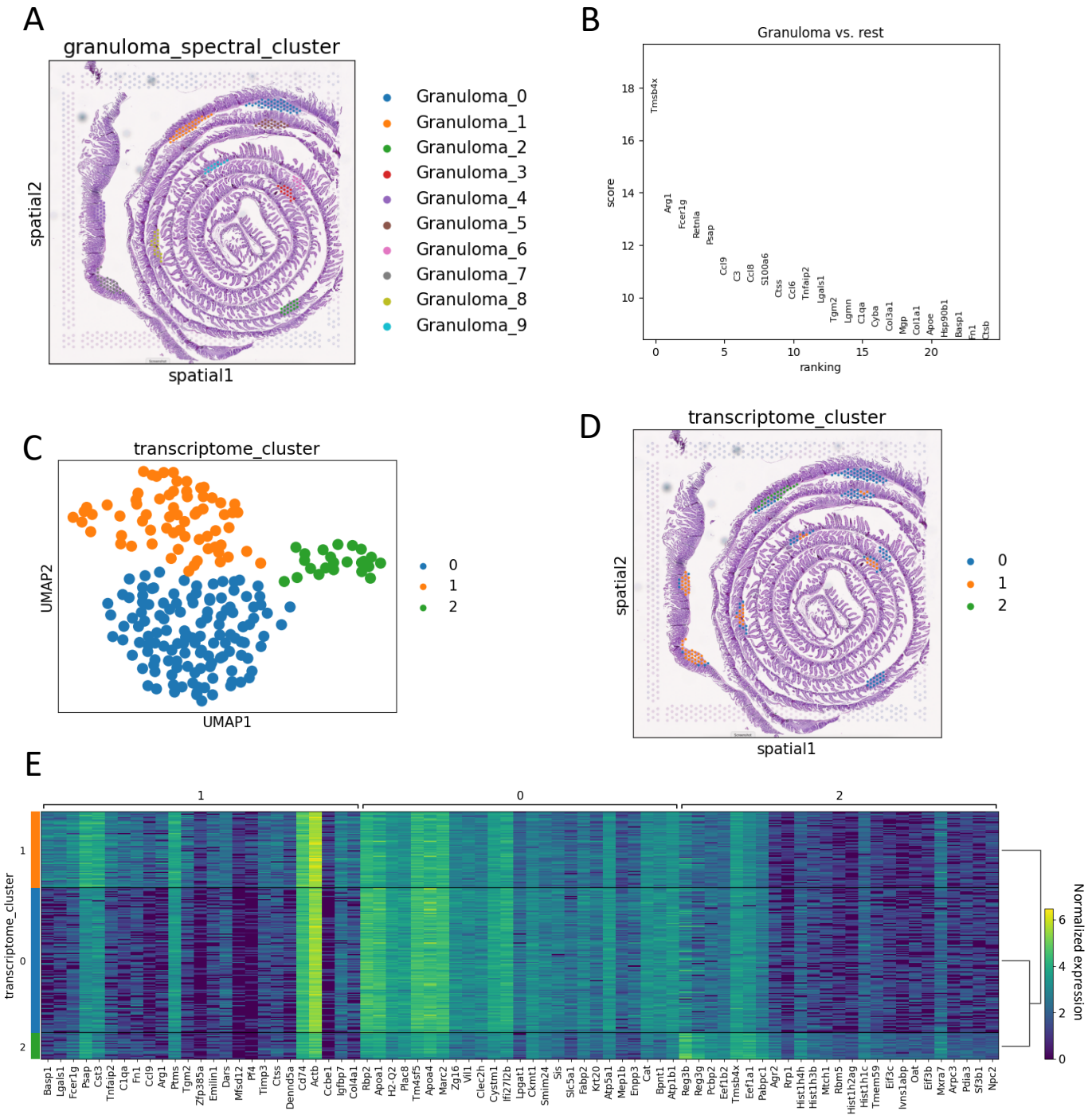

Figure 3. Characterizing transcriptomic signatures of granulomas in the intestine of *H. polygyrus* infected mice. A) Visium slide of mouse intestine 7 days post infection with *H. polygyrus* with spots coloured by which granuloma they are part of. B) The SCANPY top 25 scoring marker genes of Granuloma spots when compared to non-granuloma spots C) UMAP of Visium mouse intestine 7 days post infection with *H. polygyrus* with spots coloured by transcriptome-based Leiden cluster. D) Visium slide of mouse intestine 7 days post infection with *H. polygyrus* with spots coloured transcriptome-based Leiden clusters. E) Heatmap showing normalized gene expression of the Scanpy top 25 scoring marker genes for each of the granuloma Leiden clusters.

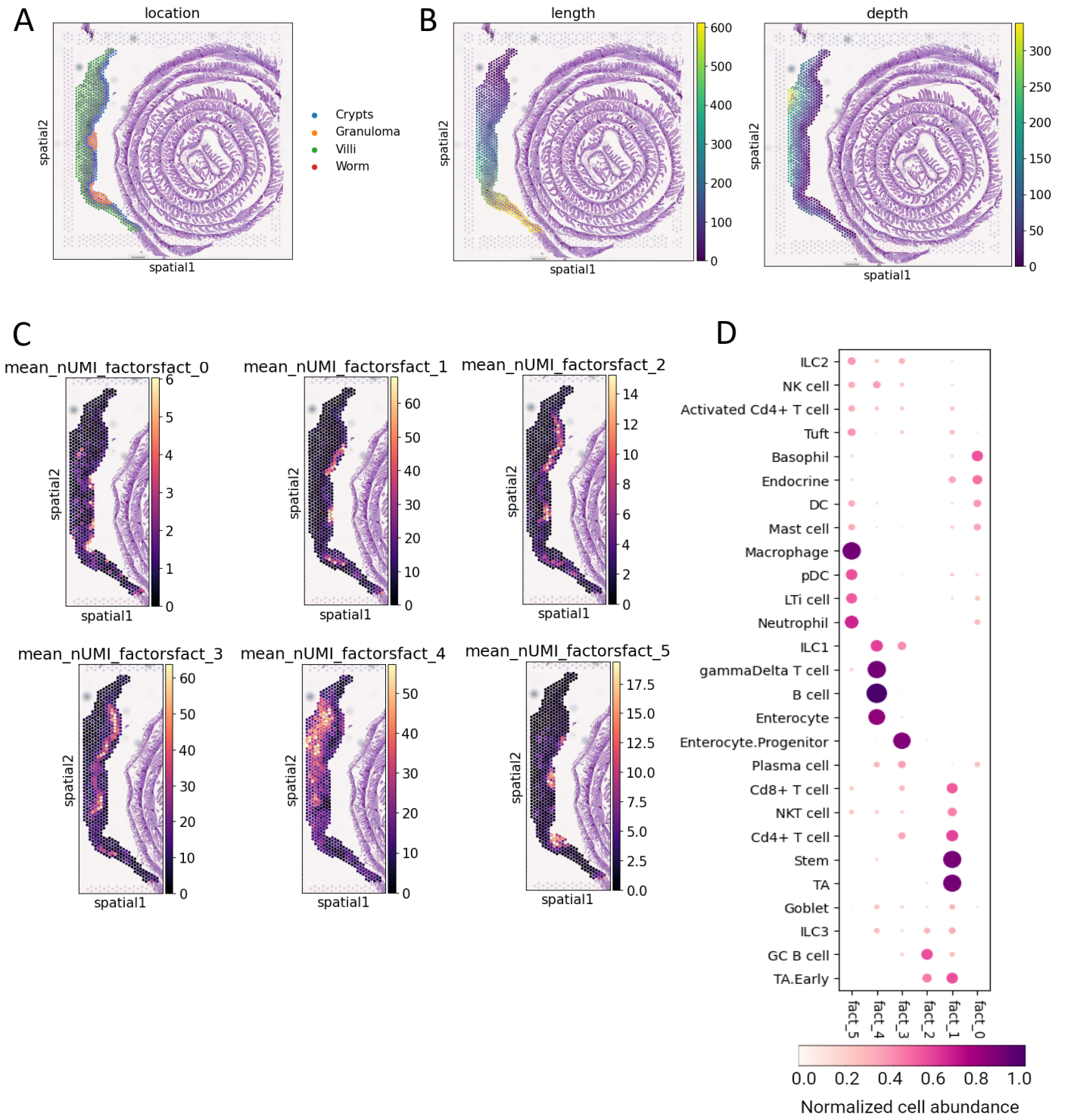

Figure 4: Spatial colocalization of cell types within *H. polygyrus* infected mouse intestine. A) Visium slide of mouse intestine 7 days post *H. polygyrus* coloured by the tissue metadata. B) Visium slides of mouse intestine 7 days post *H. polygyrus* showing the localisation of the factors within the tissue, with each spot coloured by the recreated length (left) or depth (right) axis. C) Visualization of NMF factor distribution across spots in the mice gut presenting *H. polygyrus* granulomas. Each spot is coloured by the mean UMI count for the different factors. D) Dot plot showing the contribution of different cell types to the non-negative matrix factorization factors, with each dot plot coloured by a cell type normalized cell abundance across the factors.

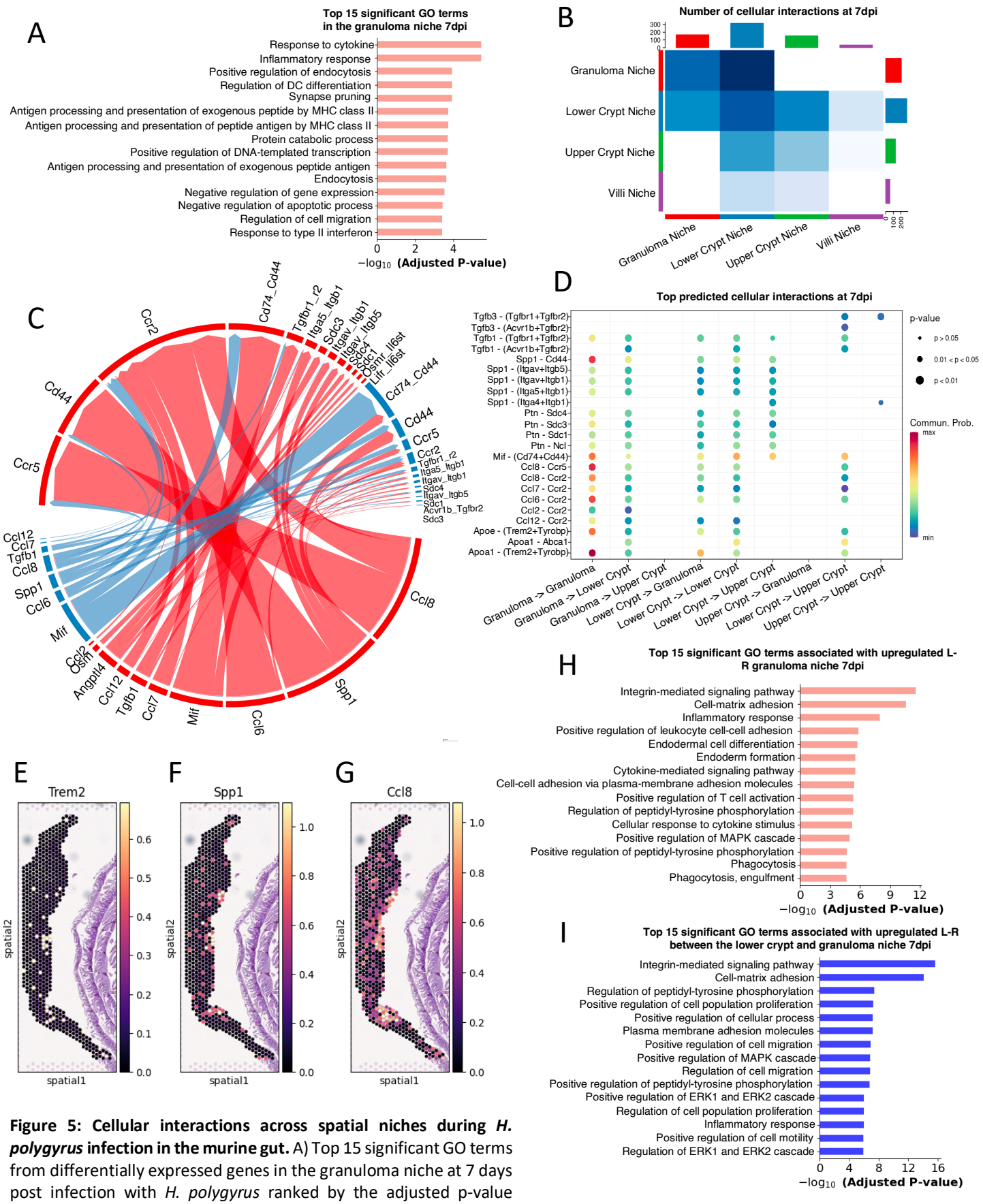

Figure 5: Cellular interactions across spatial niches during *H. polygyrus* infection in the murine gut. A) Top 15 significant GO terms from differentially expressed genes in the granuloma niche at 7 days post infection with *H. polygyrus* ranked by the adjusted p-value (<0.05). B) Number of ligand-receptor (L-R) interactions inferred by CellChat for each spatial niche at 7 days post infection. Barplots show the sum of all interactions plotted in the heatmap. C) Circos plot visualisation showing the upregulated ligand and receptors between the granuloma (red) and the lower crypt (blue) niche. Arrows show directionality of the interaction. D) Dotplot showing the communication probability of each significant ligand receptor interaction between various spatial niches in the murine gut at 7 days post infection. E-F) Spatial plots showing the distribution of transcriptomic expression of key regulators of inflammation co-localising to the granuloma niche. H) Top 15 significant GO terms from differentially expressed ligand receptors in the granuloma niche at 7 days post infection with *H. polygyrus* ranked by the adjusted p-value (<0.05). I) Top 15 significant GO terms from differentially expressed ligand receptors between the granuloma and lower crypt niche at 7 days post infection with *H. polygyrus* ranked by the adjusted p-value (<0.05)